Cement and Concrete Research 41 (2011) 324–329

Contents lists available at ScienceDirect

Cement and Concrete Research

journal homepage: http://ees.elsevier.com/CEMCON/default.asp

Structural characteristics and hydration kinetics of modified steel slag

Jianxin Li, Qijun Yu, Jiangxiong Wei *, Tongsheng Zhang

School of Materials Science and Engineering, South China University of Technology, Guangzhou, 510640, People's Republic of China
Key Laboratory of Specially Functional Materials of the Ministry of Education, South China University of Technology, Guangzhou, 510640, People's Republic of China

ARTICLE INFO

Article history:
Received 12 June 2010
Accepted 29 November 2010

Keywords:
Modified steel slag
Admixture D
Hydration A
Microstructure B
Mechanical properties C

ABSTRACT

This study investigates the structural characteristics and hydration kinetics of modified basic oxygen furnace steel slag. The basic oxygen furnace steel slag (BOFS) was mixed with electric arc furnace steel slag (EAFS) in appropriate ratios and heated again at high temperature in the laboratory. The mineralogical and structural characteristics of both BOFS and modified steel slag (MSS) were characterized by X-ray diffraction, optical microscopy, scanning electron microscopy, Raman and Fourier transform infrared spectroscopies. The results show that modification increases alite content in MSS and decreases alite crystal size with the formation of C_6AF_2. One more obvious heat evolution peak appears in MSS's heat-flow rate curves in comparison to BOFS, becoming similar to that of typical Portland cement paste. As a result, its cementitious activity is much improved.

1. Introduction

Steel slag is a by-product from either the conversion process of iron to steel in a basic oxygen furnace (BOF), or the melting of scrap to make steel in an electric arc furnace (EAF) [1]. The global amount of steel slag has increased continuously. In 2002, about 50 million tons of steel slag was produced worldwide [2], but today nearly 80 million tons of steel slag is discharged every year in China alone. The chemical compositions of steel slags vary greatly with the raw materials and process used, but generally fall within the range CaO 45–60%, SiO_2 10–15%, Al_2O_3 1–5%, Fe_2O_3 3–9%, FeO 7–20%, and MgO 3–13% by mass [3]. The presence of C_3S, C_2S, C_4AF and C_2F in steel slag makes it potentially usable as a cementitious material, but due to its low C_3S content it gives lower strengths than typical Portland cement clinkers [4]. Cement blended with steel slag usually has a longer setting time and lower early strength, and sometimes shows a larger volume expansion due to a high content of dead-burned free-CaO [5,6]. Therefore, steel slag has not yet found a wide application as a cementitious material in concrete. Steel slag is well characterized as there is a long-term experience with its use as aggregate for road construction in Europe. Owing to the intensive research work during the last 30 years about 65% of available steel slag is now used in qualified applications [7]. However, in China, only 10% of steel slag is currently reused [8], while the large volumes that go unused are stored externally leading to emission of various poisonous elements that can contaminate groundwater, water and also soil (due to the dust). Many activation approaches, such as mechanical [9], thermal [10,11] or chemical methods [12], have been used for improving the cementitious performance of steel slag. These techniques are referred to as “back-end modification techniques”, in which additional energy and chemical activators are usually needed, and the modification effect varies with the chemical and mineral compositions of steel slag.

Molten basic oxygen furnace slag contains much heat and has good fluidity. By adding some mineral admixtures to the molten slag during the discharging process, it is possible to increase the content of cementitious minerals in the product, resulting in improved hydraulic activity. Fig. 1 is the schematic diagram of the modification process in steelworks. In this study, this process was simulated in laboratory, and the structural characteristics and hydration kinetics of the modified steel slag were investigated.

2. Experimental

2.1. Materials

The basic oxygen furnace steel slag (BOFS) used in the experiment was from the Shaoguan Iron and Steel Company of China. The electric arc furnace steel slag (EAFS) used as composition adjusting material was from the same company. BOFS and EAFS were dried, crushed and ground to Blaine specific surface areas of 415 and 420 m^2/kg [13], respectively. The cement used was an ordinary Portland cement (OPC) with a Blaine specific surface area of 346 m^2/kg. The chemical compositions of the raw materials are shown in Table 1, from which it can be seen that BOFS contains more iron oxide and less CaO than OPC, while EAFS has more CaO and SiO_2 but less iron oxide than BOFS.

Fig. 2 shows that BOFS is mainly composed of alite, belite, calcium ferrite, calcium oxide and RO phase, the latter being a solid solution between MgO (periclase) and FeO (wustite). The phases observed

---

* Corresponding author. Wushan Road 381, Tianhe District, Guangzhou, 510640, People's Republic of China. Tel.: +86 20 8711 4137; fax: +86 20 8711 4233.
E-mail address: jxwei@scut.edu.cn (J. Wei).

0008-8846/$ – see front matter © 2010 Elsevier Ltd. All rights reserved.
doi:10.1016/j.cemconres.2010.11.018

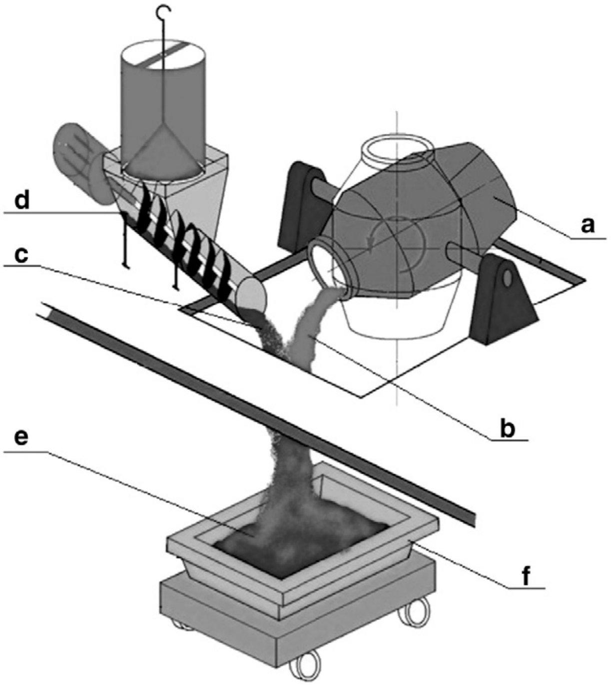

Fig. 1. Schematic illustration of the modification process in steelworks: (a) converter; (b) melting steel slag; (c) adjusting materials; (d) conveyer; (e) modified steel slag and (f) steel slag ladle.

in EAFS are γ-C_2S, periclase, anorthite, merwinite and gehlenite, with γ-C_2S being predominant.

2.2. Experimental methods

Fig. 3 shows the location of BOFS, EAFS, OPC, Portland cement clinker and modified steel slag (MSS) in a $CaO–Al_2O_3–SiO_2$ ternary phase diagram. BOFS and EAFS are located in the $C_2S–C_3A–C_{12}A_7$ and $C_3S–C_2S–C_3A$ triangles, respectively. With 10–20% by mass EAFS addition to BOFS (S_{10}, S_{15} and S_{20}), the chemical composition of the mixture, MSS, lies in the $C_3S–C_2S–C_3A$ triangle, entering into the same composition region as Portland cement clinker. Therefore, if sufficient heat is available, it is possible to form clinker phases such as alite, calcium aluminate and calcium alumino-ferrite from such compositions.

The mixtures of BOFS and EAFS with the proportions shown in Table 2 were calcined in a Si–Mo oven at the designated temperatures for 30 min. The calcined specimens were quickly cooled to room temperature after taking out from the oven, and then characterized by qualitative and quantitative X-ray diffraction (XRD and QXRD), scanning electron microscopy (SEM) and optical microscopy. The mineralogical phases of BOFS and EAFS, determined by means of a Philips X'Pert Pro diffractometer with nickel-filtered $CuK_{\alpha 1}$ (λ = 1.5406 Å, 40 kV and 40 mA), are given in Fig. 2. The determination of the mineralogical phases of MSS was carried out using the same X-ray diffractometer with iron-filtered $CuK_{\alpha 1}$ (λ = 1.7929 Å, 40 kV and 40 mA). K-value method was adopted to ascertain the amount of cementitious minerals in BOFS and MSS according to the previous report [14], and α-Al_2O_3 was used as the internal standard.

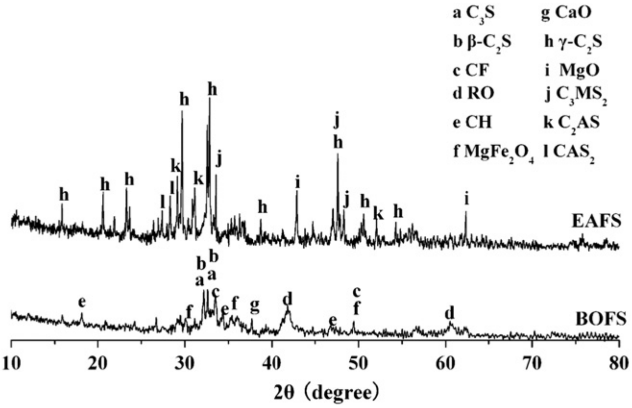

Fig. 2. XRD patterns of BOFS and EAFS (Cu $K_{\alpha 1,}$ λ = 1.5406 Å, 40 kV and 40 mA).

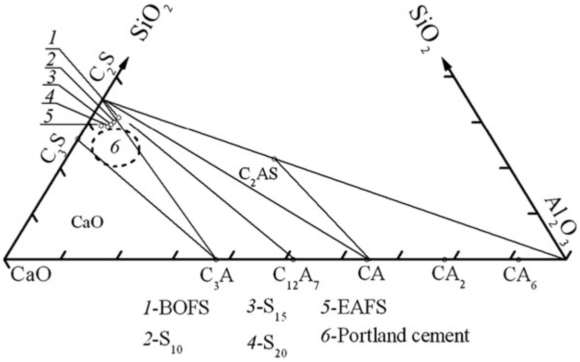

Fig. 3. Location of BOFS, S_{10}, S_{15}, S_{20}, EAFS, Portland cement clinker and OPC in a $CaO–Al_2O_3–SiO_2$ ternary phase diagram.

The ground *j* phase (pure tricalcium silicate or dicalcium silicate) and *s* phase (α-Al_2O_3) were uniformly mixed at a mass ratio of 1:1 in a mortar with ethanol. One non-overlapping X-ray diffraction peak of *j* phase and *s* phase was chosen. I_j and I_s are the integral intensity of the diffraction peak of *j* phase (C_3S or C_2S) and that of *s* phase, respectively. K_j^s is defined as follows:

$$K_j^s(C_3S) = \frac{I_j(C_3S)}{I_s};\ K_j^s(C_2S) = \frac{I_j(C_2S)}{I_s}. \tag{1}$$

According to Eq. (1), $K_j^s(C_3S)$ and $K_j^s(C_2S)$ equal to 0.54 and 0.17, respectively.

The mixed powders with α-Al_2O_3 to BOFS or MSS at a mass ratio of 15:85, as checked specimens, were homogeneously mixed. The mass fraction of a phase in the mixture was calculated by Eq. (2).

$$w'j = \frac{I_j}{I_s}\cdot\frac{1}{K_j^s}\cdot\frac{w_s}{1-w_s}, w_s = 15\% \tag{2}$$

where $w'j$ is the mass fraction of *j* phase (C_3S or C_2S) in BOFS or MSS; I_j and I_s equal to the integral intensity of the diffraction peak of *j* phase (C_3S or C_2S) and that of *s* phase in the checked specimens.

Table 1
Composition of OPC, BOFS and EAFS/mass%.

Sample	CaO	SiO_2	Al_2O_3	Fe_2O_3	FeO	Fe	MgO	SO_3	P_2O_5	Free-CaO	Loss	Total	Molar C/S
OPC	63.42	21.16	4.90	5.18	–	–	1.37	2.45	–	–	1.29	99.77	–
BOFS	40.01	18.94	2.91	8.85	13.5	1.22	5.36	0.35	1.07	1.00	2.01	95.22	2.26
EAFS	53.31	22.97	2.08	–	1.07	–	7.79	0.44	0.05	0.08	3.53	94.13	2.49

Notes: –, undetected.

Table 2
Mix proportion and calcining temperature of BOFS and EAFS.

Sample	BOFS/mass%	EAFS/mass%	Calcining temperature/°C	Chemical composition of the mixtures/mass%							Molar
				CaO	SiO_2	Al_2O_3	Fe_2O_3	FeO	Fe	MgO	C/S
$S_{10\text{-}1250}$	90	10	1250	41.34	19.34	2.83	7.97	12.26	1.10	5.60	2.29
$S_{10\text{-}1300}$	90	10	1300								
$S_{10\text{-}1350}$	90	10	1350								
$S_{15\text{-}1250}$	85	15	1250	42.01	19.54	2.79	7.52	11.64	1.04	5.72	2.30
$S_{15\text{-}1300}$	85	15	1300								
$S_{15\text{-}1350}$	85	15	1350								
$S_{20\text{-}1250}$	80	20	1250	42.67	19.75	2.74	7.08	11.01	0.98	5.85	2.31
$S_{20\text{-}1300}$	80	20	1300								
$S_{20\text{-}1350}$	80	20	1350								

The content of alite and belite in BOFS and MSS calculated according to Eq. (2) is shown in Table 3.

Both BOFS and MSS specimens for optical microscopy observation were etched with 1% NH_4Cl aqueous solution after sulfur casting and polishing, then their microstructure was examined using an optical microscope (Leica DM2500P), the images are shown in Fig. 5. Morphological observations of BOFS and MSS were made by SEM (NanoSEM 430, 15 kV) and are shown in Fig. 6. Micro-area compositions of BOFS and MSS were determined by X-ray energy dispersive spectroscopy (EDS, Oxford 7573, 20 kV).

The Si–O, Fe–O and C–O vibrational bands in BOFS and MSS were identified by Raman and Fourier transform infrared spectroscopies (FTIR). Raman microspectrometry analyses were carried out on ground slag powder using a Labram Aramis instrument (Jobin Yvon Horiba group) with an internal He–Ne laser ($\lambda = 632.8$ nm). FTIR analyses were made with a Vector 33(Bruker group) instrument using potassium bromide pellets (sample: KBr = 1:50).

In addition, the hydration kinetics of BOFS and MSS pastes with water/solids ratios of 0.4 was studied for up to 72 h at 25 ± 1 °C using an isothermal calorimeter (TAM Air, Thermometric AB, Sweden). Mortar bars (40 × 40 × 160 mm) were cast with binder, sand, and water in a mass ratio of 1:3:0.5, in which the binding material was composed either of 100% OPC, or of blends of 70% OPC and 30% ground MSS or 30% BOFS by mass, respectively. After 24 h, the specimens were demoulded and cured in tap water at 20 ± 1 °C for 3, 7 and 28 days.

3. Results and discussion

3.1. Change of mineralogical composition

Results in Fig. 4 show that all of the MSS compositions made in this work are composed mainly of alite, belite, C_2F, C_6AF_2, C_2AS, magnetite and magnesioferrite. The major phase in EAFS is γ-C_2S, and this can be transformed to β-C_2S by incorporation of ions such as Fe^{3+}, Mg^{2+} and Al^{3+} at high temperatures, (and then stabilized by fast cooling). Furthermore, β-C_2S can combine with calcium oxide to form alite. Table 3 shows that after modification alite content is increased by 7.3–12.7%, while belite content is decreased by 2–5%. An addition of EAFS to BOFS increases the quantity of calcium oxide but it also increases the quantity of silica. However, Table 2 shows that EAFS addition produces a net increase in C/S molar ratio (from 2.26 to 2.31) of the mixtures, which should lead to an increase in the alite/belite ratio amount.

Table 3
Mass fraction of different phases in checked sample by QXRD.

Sample	Mass%	
	Alite	Belite
BOFS	8.2 ± 0.3	38.2 ± 1.3
$S_{15\text{-}1250}$	15.5 ± 0.7	36.3 ± 1.1
$S_{15\text{-}1300}$	17.9 ± 0.9	34.2 ± 1.2
$S_{15\text{-}1350}$	20.9 ± 1.0	33.5 ± 1.1

The amount of C_3A in MSS must be very low because its characteristic peaks are not observed in XRD patterns. The formation of C_6AF_2 in MSS is due to the combination of aluminate phase and ferrite phase at elevated temperature. A part of the iron oxide in the mixture BOFS and EAFS combines with calcium oxide and forms C_2F when heated in air. At the same time other iron-rich phases including RO phase tend to give magnetite [15] and magnesioferrite ($MgO \cdot Fe_2O_3$), respectively.

3.2. Microstructure, morphological observation and micro-area chemical analysis

The optical micrographs of BOFS and MSS are shown in Fig. 5. In MSS calcined at 1250 °C, alite crystals are angular or rectangular, while belite crystals are rounded or elliptical in shape, both having

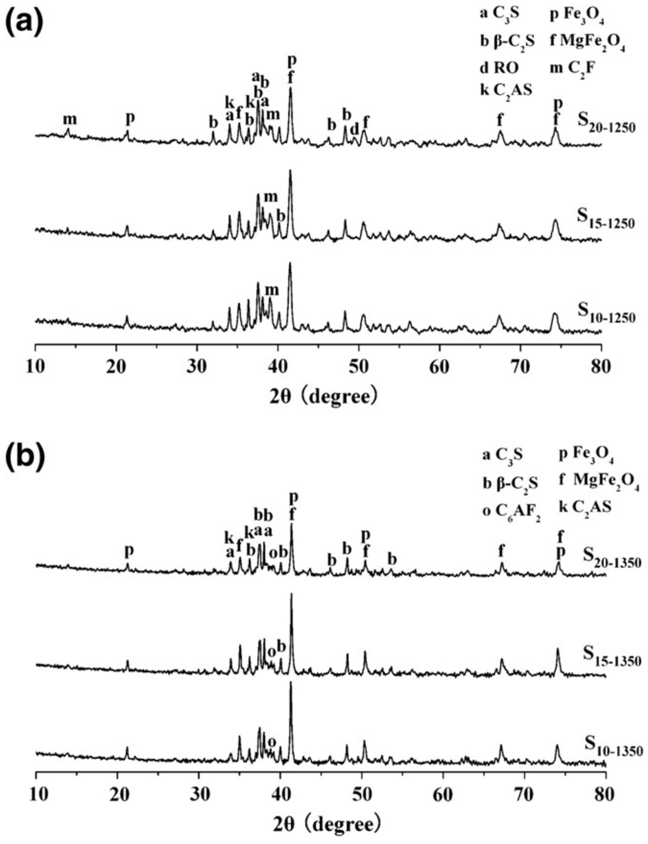

Fig. 4. XRD patterns of MSS with different additions of EAFS (Cu $K_{\alpha 1}$, $\lambda = 1.7929$ Å, 40 kV and 40 mA): (a) modification at 1250 °C; (b) modification at 1350 °C.

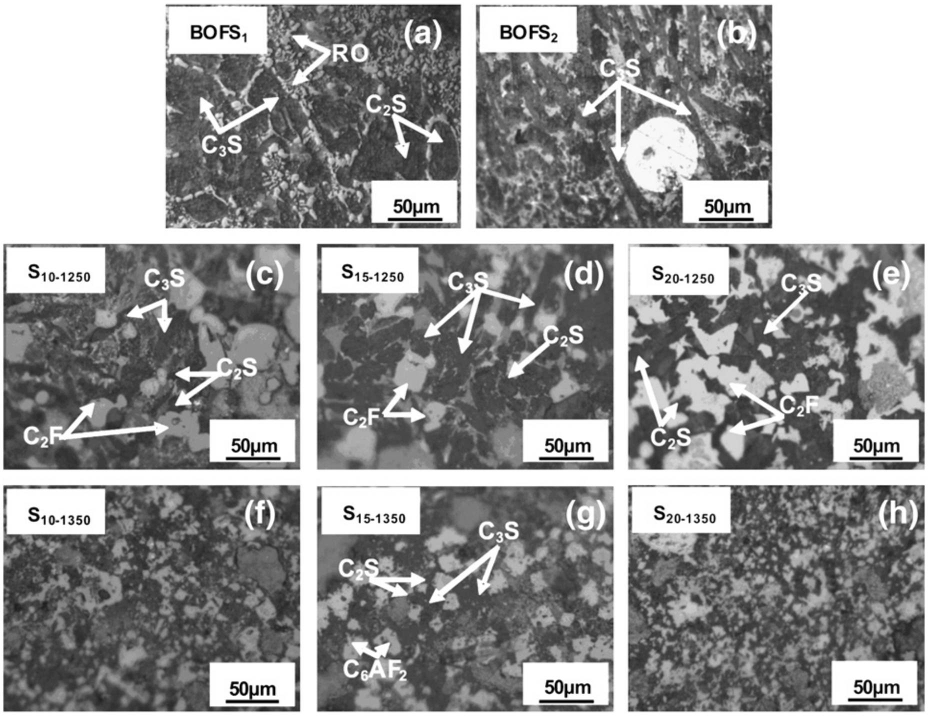

Fig. 5. Reflected optical microcopy photos of BOFS and MSS: (a, b) BOFS; (c, d and e) MSS at 1250 °C; (f, g and h), MSS at 1350 °C.

more regular shapes than those in BOFS. The average size of alite crystals is about 20–50 μm after modification, with the amount being increased by 10–15% according to area calculation.

Fig. 6 shows the scanning electron micrographs of BOFS and MSS, in which area *a*–area *b′* denote the areas analyzed by EDS. The results in Tables 4–5 indicate that after modification, RO phase transforms to magnesioferrite ($MgO \cdot Fe_2O_3$), and at the same time the amount of Fe^{3+}, Mg^{2+} and Al^{3+} incorporated into alite is likely increased.

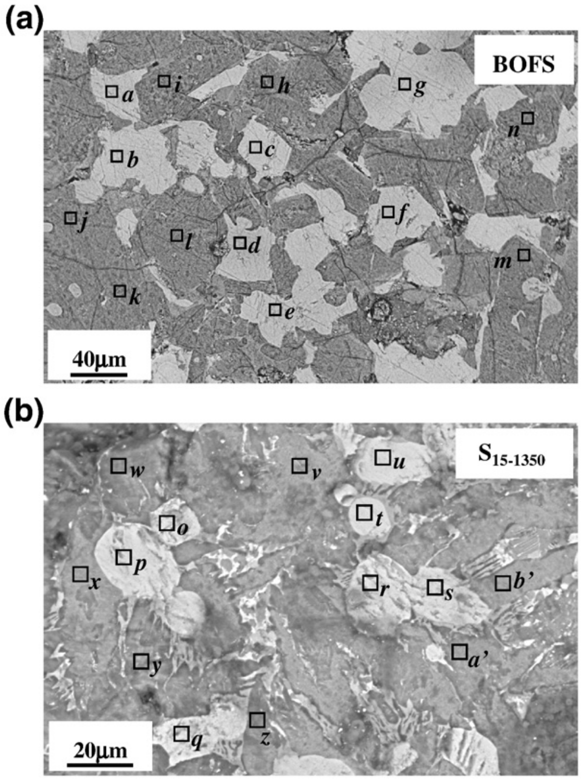

Fig. 6. Selected areas in EDS analysis of BOFS and MSS: (a) BOFS; (b) $S_{15\text{-}1350}$.

3.3. Raman and FTIR spectroscopy analyses of BOFS and MSS

Fig. 7 shows the Raman spectra of BOFS and $S_{15\text{-}1350}$ samples. In BOFS, the Raman shifts at 682 cm^{-1} and 955 cm^{-1} correspond to belite in reducing condition and a v_1 SiO_4 vibration of β-C_2S respectively; the results are consistent with the studies of Bonen [16] and Bensted [17]. In $S_{15\text{-}1350}$, the intensity at a Raman shift of 848 cm^{-1} corresponding to tricalcium silicate becomes stronger; but the intensities at Raman shifts of 682 and 955 cm^{-1} become weaker, which shows that the content of belite (β-C_2S) decreases and that of alite increases in comparison to BOFS. Magnesioferrite in $S_{15\text{-}1350}$ is assigned to the Raman shifts at 705 and 523 cm^{-1} [17].

Fig. 8 gives the typical FTIR spectra of BOFS and MSS samples. IR spectra can identify silicates as the most abundant components, with absorption bands 519(v_4), 915, and 993(v_3) cm^{-1} assigned to alite [18]. The absorption peaks at 584, 847 and 1448 cm^{-1} correspond to v (Fe–O) of magnetite, SiO_4^{4-} bending vibration of β-C_2S and v_3 CO_3^{2-} being the effect of carbon dioxide, respectively. Compared with BOFS, the absorption bands corresponding to alite become stronger, but the absorption bands corresponding to belite become weaker in MSS. In BOFS, the absorption bands at 1634 cm^{-1} and 3642 cm^{-1} match with OH^- bending vibration for water and calcium hydroxide respectively, and after calcining, the hydroxide groups disappear. The results of Raman and FTIR spectra accord with those of X-ray diffraction in Section 3.1.

3.4. Hydration kinetics of BOFS and MSS

Fig. 9a shows a single heat evolution peak for BOFS within a few minutes of mixing and no other detectable peaks over the next 3 days, while the calorimetric curve of MSS is more similar to that of typical Portland cement paste or C_3S paste, having one early (but short duration) heat evolution peak followed by a second peak of longer duration within the 3-day period studied. The second exothermic

Table 4
Results of X-ray energy dispersive spectroscopy (EDS) of RO phase in BOFS and ($MgO\cdot Fe_2O_3$) in $S_{15\text{-}1350}$.

	BOFS/mass%							$S_{15\text{-}1350}$/mass%						
	a	*b*	*c*	*d*	*e*	*f*	*g*	*o*	*p*	*q*	*r*	*s*	*t*	*u*
MgO	38.4	36.3	38.9	35.9	39.9	39.5	37.6	10.7	10.8	11.2	10.3	10.4	10.7	10.2
CaO	2.5	3.4	1.6	2.8	2.5	2.0	3.4	1.1	2.4	1.2	1.6	1.3	1.4	1.7
MnO	4.0	4.1	3.3	4.1	3.7	3.8	4.7	2.9	2.8	2.7	2.6	3.3	3.1	2.3
FeO	55.1	56.2	56.2	57.2	53.9	54.7	54.3	–	–	–	–	–	–	–
Fe_2O_3	–	–	–	–	–	–	–	85.3	84.0	84.9	85.5	85.0	84.8	85.8

Notes: –, undetected; the chemical compositions of area *a*–*g* corresponding to RO phase in BOFS; the chemical compositions of area *o*–*u* corresponding to $MgO\cdot Fe_2O_3$ in $S_{15\text{-}1350}$.

Table 5
Results of X-ray energy dispersive spectroscopy (EDS) of alite in BOFS and $S_{15\text{-}1350}$.

	BOFS/mass%							$S_{15\text{-}1350}$/mass%						
	h	*i*	*j*	*k*	*l*	*m*	*n*	*v*	*w*	*x*	*y*	*z*	*a′*	*b′*
Al_2O_3	1.3	1.7	1.4	1.2	1.5	1.4	1.3	2.5	1.9	2.3	2.6	2.2	2.1	2.8
SiO_2	29.9	28.6	29.8	29.5	30.1	29.3	30.7	24.6	25.8	25.1	25.3	25.9	25.7	26.0
CaO	66.7	67.7	66.9	67.5	66.6	67.3	66.1	66.8	66.5	67.1	65.7	66.2	66.7	65.8
Fe_2O_3	1.87	1.69	1.65	1.67	1.62	1.78	1.73	3.8	3.7	3.1	3.9	3.0	3.5	3.2
MgO	0.23	0.31	0.25	0.33	0.18	0.22	0.17	2.3	2.1	2.4	2.5	2.7	2.0	2.2

Notes: the chemical compositions of area *h*–*n* corresponding to alite in BOFS; the chemical compositions of area *v*–*b′* corresponding to alite in $S_{15\text{-}1350}$.

peak of $S_{15\text{-}1250}$, $S_{15\text{-}1300}$ and $S_{15\text{-}1350}$ is attributed to the hydration of alite formed in MSS.

The cumulative hydration heat evolution curves of OPC, BOFS and MSS are shown in Fig. 9b. The cumulative hydration heats of BOFS, $S_{15\text{-}1250}$, $S_{15\text{-}1300}$ and $S_{15\text{-}1350}$ are 10.2 J g^{-1}, 22.2 J g^{-1}, 29.7 J g^{-1} and 35.5 J g^{-1} after 72 h, respectively, showing that the cumulative hydration heat of $S_{15\text{-}1350}$ is 2.5 times greater than that of BOFS, although still far less than that of the OPC (around 200 J g^{-1}). The increase in cumulative hydration heat of MSS results from the change in the amount and size of alite, as well as the formation of C_6AF_2.

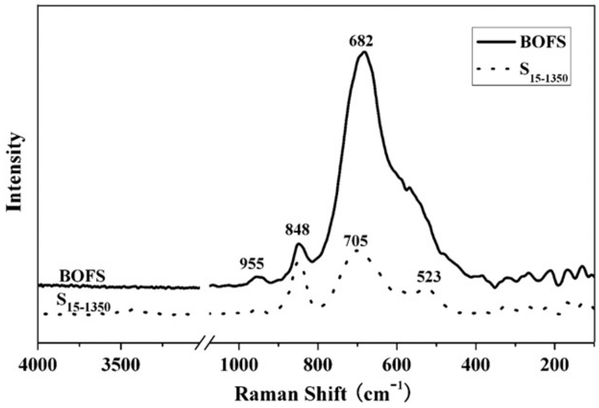

Fig. 7. Raman spectra of BOFS and $S_{15\text{-}1350}$ obtained with 632.8 nm excitation.

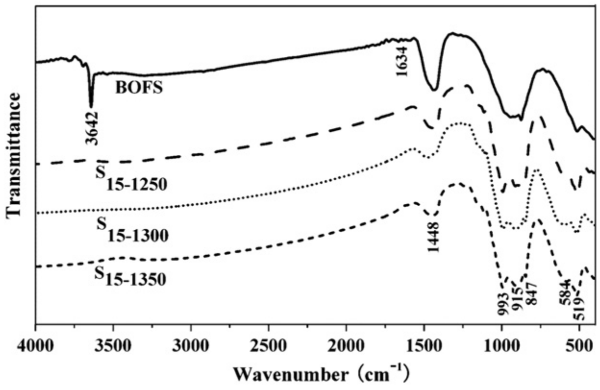

Fig. 8. IR spectra of BOFS, $S_{15\text{-}1250}$, $S_{15\text{-}1300}$ and $S_{15\text{-}1350}$.

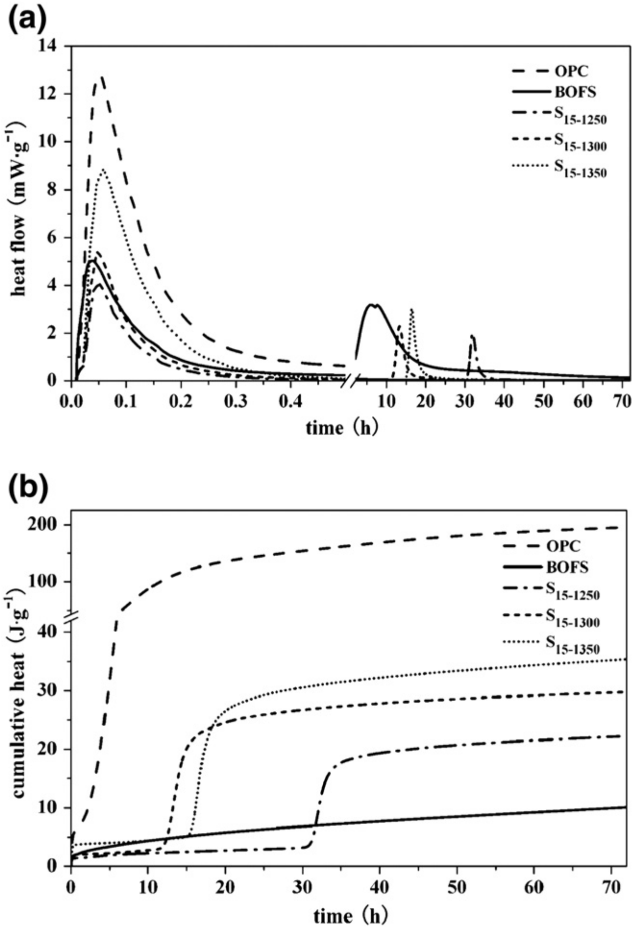

Fig. 9. Hydration heat evolution curves of OPC, BOFS and MSS: (a) rate of heat evolution of OPC, BOFS and MSS; (b) cumulative heat of OPC, BOFS and MSS.

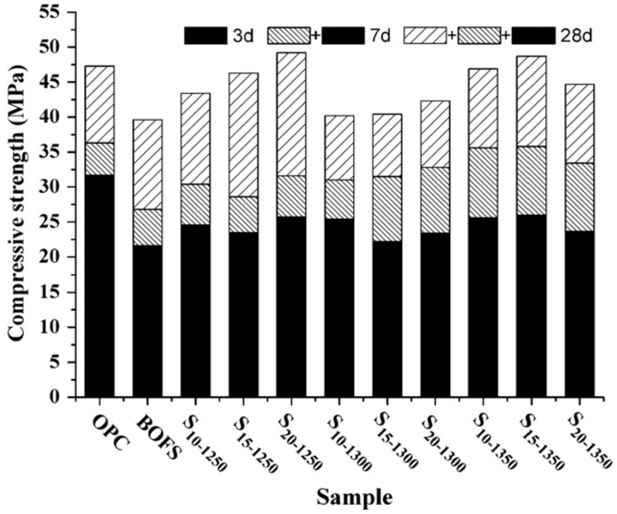

Fig. 10. Compressive strength of cement (OPC), cement with ground BOFS and ground MSS cured for various ages.

3.5. Compressive strength of cement mortar with MSS replacement

Fig. 10 shows that the compressive strength of cement mortars incorporating 30% ground MSS by mass as a replacement for cement is greater than that of BOFS samples at all ages. In addition, the compressive strength of the mortars incorporating 30% by mass ground $S_{20\text{-}1250}$ and $S_{15\text{-}1350}$ as replacement for cement reaches 49.2 and 48.7 MPa at 28 days, being 21% and 20% higher than that of BOFS samples and superior to that of the ordinary Portland cement used in the experiment. It is well known that the cementitious activity of steel slag strongly depends on the content and crystal size of alite. With the increment of alite content and reduction in alite crystal size, the cementitious activity of MSS is certainly improved. Furthermore, C_6AF_2, as a newly-formed cementitious phase in MSS, also contributes to strength development.

4. Conclusions

The mineralogical composition, structure and hydration kinetics of steel slag can be modified with added electric arc furnace steel slag at high temperature, giving a modified steel slag with improved cementitious activity. Alite is increased by 7.3–12.7% in amount and decreased in crystal size. The calorimetric curves for the MSS samples are much more similar to OPC than to BOFS, i.e. they have a second peak which appears to be due to alite hydration. As a result, the cumulative hydration heat of MSS after 72 h at 25 °C increases by 2.5 times in comparison to that of BOFS. The improvement of cementitious activity of MSS is due to: (1) increased alite content; (2) smaller alite crystals; and (3) formation of cementitious C_6AF_2.

Acknowledgments

The authors are grateful to the National Science and Technology Pillar Program during the Eleventh Five-year Plan (project no. 2006BAF02A24) and the National Basic Research Program "973" Project of China (project no. 2009CB623104) for their financial support to this study.

References

[1] C.J. Shi, Steel slag—its production, processing, characteristics, and cementitious properties, J. Mater. Civil. Eng. 16 (3) (2004) 230–236.
[2] A. Altun, I. Yilmaz, Study on steel furnace slags with high MgO as additive in Portland cement, Cem. Concr. Res. 32 (8) (2002) 1247–1249.
[3] X.Q. Wu, H. Zhu, X.K. Hou, H.S. Li, Study on steel slag and fly ash composite Portland cement, Cem. Concr. Res. 29 (7) (1999) 1103–1106.
[4] C.J. Shi, J.S. Qian, High performance cementing materials from industrial slags—a review, Resour. Conserv. Recycl. 29 (3) (2000) 195–207.
[5] C.J. Shi, R.L. Day, Early strength development and hydration of alkali-activated blast furnace slag: fly ash blends, Adv. Cem. Res. 11 (4) (1999) 89–96.
[6] A. Monshi, M.K. Asgarani, Producing Portland cement from iron and steel slags and calcium oxide stone, Cem. Concr. Res. 29 (9) (1999) 1373–1377.
[7] H. Motz, J. Geiseler, Products of steel slags an opportunity to save natural resources, Waste Manage. 21 (3) (2001) 285–293.
[8] G.L. Zhu, Development and current situation of steel and iron slags, Metall. Environ. Prot. 6 (2009) 26–31, (in Chinese).
[9] Y.M. Chen, H.T. Zhang, High reactivity blending materials prepared by pulverized steel slag, Cement 5 (2001) 1–4, (in Chinese).
[10] G.R. Qian, D.D. Suna, Autoclave properties of kirschsteinite-based steel slag, Cem. Concr. Res. 32 (9) (2002) 1377–1382.
[11] C.J. Shi, S.F. Hu, Cementitious properties of ladle slag fines under autoclave curing conditions, Cem. Concr. Res. 33 (11) (2003) 1851–1856.
[12] D.X. Li, X.H. Fu, X.Q. Wu, M.S. Tang, Durability study of steel slag cement, Cem. Concr. Res. 27 (7) (1997) 983–987.
[13] Chinese Standard GB 8074-2008, Blaine Air Permeability Method for Test Cement Specific Surface Area, 2008.
[14] S.Y. Zhao, Q.J. Yu, Study on the hydration and hydration kinetics of $11CaO\cdot 7Al_2O_3\cdot CaF_2$ at different hydration temperatures, J. Wuhan Univ. Technol. 24 (8) (2002) 23–27, (in Chinese).
[15] H.F.W. Taylor, Cement Chemistry, second ed. Thomas Telford, London, 1997.
[16] S.S. Potgieter-Vermaak, J.H. Potgieter, R. Van Grieken, The application of Raman spectrometry to investigate and characterize cement, Part I: a review, Cem. Concr. Res. 36 (4) (2006) 656–662.
[17] B.E. Scheetz, W.B. White, in: McCarthy, R.J. Lauf (Eds.), Proceedings of MRS Conference on: Fly Ash and Coal Conversion By-Products: Characterization, Utilization and Disposal I, MRS, 43, 1985, p. 53.
[18] J. Setién, D. Hernández, J.J. González, Characterization of ladle furnace basic slag for use as a construction material, Constr. Build. Mater. 23 (5) (2009) 1788–1794.